Received: 8 June 2020 | Revised: 20 July 2020 | Accepted: 20 July 2020

DOI: 10.1002/VIW.20200063

MINI-REVIEW

Mass spectrometry imaging based on laser desorption ionization from inorganic and nanophotonic platforms

Laith Z. Samarah | **Akos Vertes**

Department of Chemistry, George Washington University, Washington, DC

Correspondence
Akos Vertes, Department of Chemistry, George Washington University, 800 22nd Street NW, Suite 4000, Washington, DC 20052.
Email: vertes@gwu.edu

Funding information
U.S. National Science Foundation, Plant Genome Program; Division of Integrative Organismal Systems, Grant/Award Number: IoS-1734145

Abstract

Mass spectrometry imaging (MSI) has become an important analytical tool for the label-free chemical imaging of diverse molecules in biological specimens. This minireview surveys some emerging methods in the context of factors that can lead to inaccurate information in MSI, chemical and spatial aberrations, along with their common sources. Matrix-assisted laser desorption ionization, based on organic matrices, has become the most widely used MSI technique for biomolecules. However, due to inherent limitations associated with the use of organic matrices, for example, heterogeneous matrix-analyte cocrystallization, and spectral interferences due to the matrix, laser desorption ionization (LDI) from inorganic and nanophotonic platforms has emerged as an alternative MSI modality with complementary advantages. In this review, inorganic and nanophotonic platforms for LDI-MSI, their applications in imaging, notable merits, and limitations are described.

KEYWORDS

aberrations in chemical imaging, inorganic matrices, laser desorption ionization, mass spectrometry imaging, nanophotonic ionization, nanostructures

1 | INTRODUCTION

The ability to explore the spatial distribution of chemical species in samples is key to improving our understanding of complex molecular phenomena that occur in organic (eg, biological tissues) and inorganic (eg, geological samples) systems. Several molecular imaging technologies, including fluorescence microscopy, magnetic resonance imaging (MRI), and positron emission tomography, have become indispensable in various disciplines, in particular, in biomedical and clinical applications.[1] Each of these imaging modalities can provide abundance distributions for specific molecules in biological specimens, and some of them, for example, MRI, can deliver such information in vivo and in real time.[1]

Although the frontiers of our knowledge, especially in biomedicine, have been remarkably expanded thanks to these imaging technologies, the spatial information provided by them is limited to a low number of targeted molecules. For example, immunostaining used in histology capitalizes on specific binding of antibodies or other reagents to the targeted biomolecules in the tissue. A more desired imaging technique would provide spatial measurements for untargeted molecules, in a label-free,

and multiplexed fashion (ie, report on several compounds simultaneously), without sacrificing sensitivity.

Compared to other technologies, mass spectrometry (MS) possesses a unique combination of analytical figures of merit, including high sensitivity and dynamic range, wide molecular coverage, tunable selectivity, fast analysis time, and the ability to provide structural information for molecules. Mass spectrometry imaging (MSI) simultaneously determines the spatial distributions of numerous molecules in a sample based on mapping the corresponding ion intensities.

Secondary ion MS (SIMS) was one of the earliest MSI techniques to be developed and commercialized.[2] By using a highly focused incident primary ion beam to desorb and generate secondary ions from the sample surface, the principal advantage of SIMS in MSI is its routinely high spatial resolution that can be as small as 20 nm.[2,3] However, apart from high costs and complex instrumentation, another factor that has limited the widespread use of SIMS in various MSI areas, particularly, the analysis of intact biomolecules, is the decrease in secondary ion yields for higher m/z ions primarily due to their extensive fragmentation.[3] Recent results based on large clusters as primary ions (eg, C_{60}^+ and Au_3^+) have greatly alleviated these limitations, and established cluster SIMS as a powerful tool for biomedical molecular imaging.[4]

In the wake of the pioneering work in matrix-assisted laser desorption ionization (MALDI) MS for soft ionization and analysis of intact proteins,[5] MALDI quickly became the most widely used MSI technique.[6,7] As most commercially available laser desorption ionization (LDI) MS instruments utilize wavelengths of 337 nm (nitrogen laser) and 355 nm (frequency-tripled Nd:YAG laser), organic acids with strong optical absorption at these wavelengths, such as 2,5-dihydroxybenzoic acid (DHB), have become the most frequently used matrices in MALDI. However, these organic matrices are generally detected in the same spectral range as small molecules, for example, metabolites, thus suppressing their ionization and interfering with their detection.[8] Additionally, the selection of a specific matrix in MALDI can lead to preferential ionization and detection for certain biomolecular classes in complex biological samples, thus limiting the molecular coverage.

More recently, inspired by the early use of cobalt nanoparticles (NP) and glycerol for MALDI-MS of proteins,[5] efforts were directed toward developing LDI platforms based on inorganic substrates and matrices to reduce signal interference for low-molecular-weight compounds. For the fidelity of MSI, sample preparation and MS data acquisition must not alter the native spatial distribution of molecules in the sample. Deposition of organic matrices in solution form onto the sample in MALDI can cause the spreading of analytes, altering their native distributions and reducing the spatial resolution.[9] Inhomogeneous cocrystallization of the matrix and analytes in the sample can also lead to inaccurate spatial mapping of molecules.[10]

To address these limitations in MSI, several matrix-free ionization platforms, such as LDI from inorganic substrates,[11,12-15] nanophotonic[16-18] and plasmonic[19] ionization platforms, and some atmospheric-pressure ionization methods,[20] have emerged. Recently, a wide variety of inorganic substrates for LDI have been developed, including graphite,[12,21-23] carbon nanotubes,[15,24] graphene,[25] nanodiamonds,[26] silicon nanostructures,[13,16,17,27-30] germanium,[29,31] gold and silver NP (AuNP and AgNP, respectively),[32,33,34-36] core-shell NP,[37] titanium oxide,[14,38,39,40] zinc oxide,[14,41] iron oxide,[42] laser-engineered metal-based antireflection (AR) surfaces,[43,44] and metal organic frameworks (MOFs).[45,46] Some of them, including desorption ionization on silicon (DIOS),[47] nanostructured indium tin oxide slides for surface-assisted LDI,[48] nanowire-assisted LDI,[49] silica plate imprinting LDI,[50] and LDI from laser-engineered graphene paper and polydopamine-coated AR surfaces,[44,51] have been utilized in a limited number of imaging applications. A few inorganic materials and substrates for LDI, in particular, AuNP and AgNP,[33,34,36,52-55] nanostructure-initiator mass spectrometry (NIMS),[30,56-59] and nanophotonic ionization from silicon nanopost arrays (NAPAs),[60,61] have been more broadly explored for MSI.

This minireview looks at the limitations of various MSI platforms in terms of the related spatial and chemical aberrations. Recent developments in inorganic substrates for LDI and nanophotonic ionization platforms are reported with emphasis on MSI. The different platforms, their imaging applications, figures of merit related to MSI, limitations, and special considerations for their operation in MSI are discussed. An outlook on potential directions for these emerging platforms in bioanalytical areas is given. For other areas of interest regarding these MS platforms, for example, descriptions of the different inorganic materials, synthetic protocols, desorption/ionization mechanisms, analytical figures of merit, and applications in other areas, the interested reader is directed to excellent recent reviews.[62,63]

2 | ABERRATIONS AND LIMITATIONS IN MSI

For all MSI experiments, irrespective of the imaging platform, the goal is to obtain chemical, spatial, and sometimes quantitative information on molecules in the sample

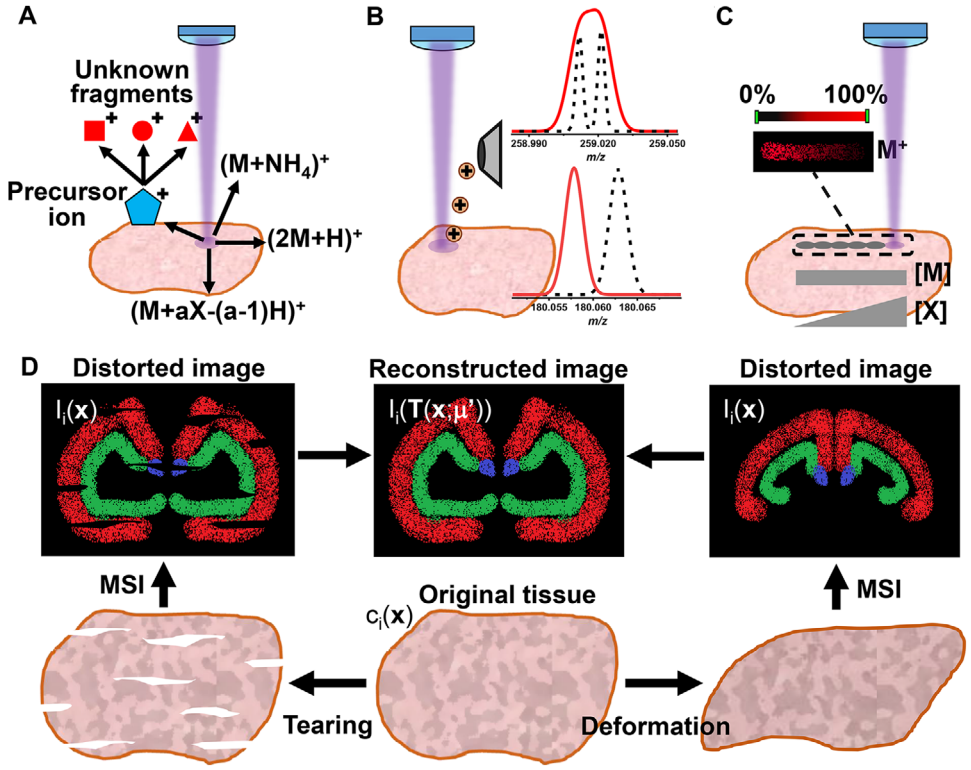

FIGURE 1 Chemical and spatial aberrations in MSI. **(A)** Two types of chemical aberrations are shown, including generation of unknown in-source fragments, and unusual adducts ("a" is a whole number and "X" is typically Na^+ or K^+). **(B)** Two types of chemical aberrations associated with mass analysis, including inaccurate m/z assignment due to poor mass resolution (top spectrum) and mass accuracy (bottom spectrum). **(C)** and **(D)** illustrate examples of spatial aberrations in MSI. **(C)** Matrix effect on the observed spatial distribution of M^+ due to heterogeneous concentrations of ion suppressing agents (X) in the sample. **(D)** Tissue section, with analyte concentration distributions, $c_i(\mathbf{x})$, can undergo tearing and deformation during sample preparation resulting in distorted ion intensity images, $I_i(\mathbf{x})$. They may be transformed to reconstruct an image, $I_i(\mathbf{T}(\mathbf{x};\boldsymbol{\mu}'))$, that represents the original spatial distribution of molecules (see text for details)

without compromising their original spatial concentration distributions, $c_i(\mathbf{x})$, for all components of interest, i, where $\mathbf{x}$ is a position vector pointing to an imaging voxel in the tissue. In MSI, the measured ion intensity distributions, $I_i(\mathbf{x})$, are distorted by spatial and chemical aberrations. Similar to aberrations that occur in optical systems, for example, spherical and chromatic aberrations, deviations from the true spatial distributions of molecules in a sample during MSI and impediments in molecular assignments can be considered as aberrations in the chemical sense. Here, two types of aberrations in MSI are considered, spatial and chemical aberrations (see Figure 1). These can come from four key sources, the instrumentation, MSI ionization platform, sample preparation, and the sample itself (see Figure 1). Understanding the potential causes behind these aberrations and developing corrective measures are necessary for obtaining accurate chemical, spatial, and quantitative information in MSI. In this section, spatial and chemical aberrations that are often encountered in MSI are discussed, along with the factors that can cause them.

2.1 | Chemical aberrations

Chemical aberrations refer to processes that obscure the identification of compounds in a sample or alter the corresponding ion intensities. Sometimes, such aberrations can be accounted for by a functional relationship, $F(I_i(\mathbf{x}), \ldots, I_j(\mathbf{x}))$, which connects a subset of ion intensities to the concentration of a particular species, $c_i(\mathbf{x}) = F(I_i(\mathbf{x}), \ldots, I_j(\mathbf{x}))$. For example, fragmentation of a molecular ion results in a set of fragment ion intensities that summed together can correlate with the concentration of the related molecule in the tissue. These aberrations stem mainly from instrumental factors that begin at the ionization source and extend to mass analysis, including in-source ion fragmentation, complex-adduct/ion formation, and poor mass accuracy and resolution (see Figures 1A and 1B). Biochemical changes that occur during, and sometimes, due to, sample preparation are another major source of chemical aberrations. For example, the glutathione to oxidized glutathione concentration ratio in mammalian cells (iBMK) is ~170.[64] During sample preparation in

ambient environment, this ratio can be dramatically suppressed due to the presence of oxygen in the air.

2.1.1 | Instrumental factors that lead to chemical aberrations

Chemical aberrations associated with instrumentation usually begin at the ion source and involve physical and chemical processes that complicate the assignment of chemical species. In-source fragmentation is one such process that can obscure molecular assignments in cases where it results in complete elimination of the precursor ion and production of unknown fragment ions (see Figure 1A). This can occur in some inorganic and nanophotonic LDI platforms in case of higher laser fluences compared to conventional MALDI. Inferring chemical images for the intact ions from the spatial distribution of the fragments is often misleading as it requires knowledge of the fragmentation products, their potential precursors, and the extent of in-source fragmentation.

Adduct ion formation, for example, $(M+2K\text{-}H)^+$, $(M+2Na\text{-}H)^+$, $(M+K+Na\text{-}H)^+$, and $(2\ M+H)^+$, where M corresponds to the molecular species, is another process that can complicate peak assignments, and is often observed in inorganic LDI platforms (see Figure 1A). This can be especially problematic for the identification of unknown compounds, which often requires several orthogonal methods, for example, tandem MS and ion mobility data. Additionally, determining all ionic forms for a given molecular species and combining their intensities are essential for quantitative MSI.

Limitations on molecular coverage are part of the chemical aberrations for LDI-MSI based on inorganic and nanophotonic platforms. In particular, although many of these platforms exhibit enhanced ionization for small molecules and certain lipid classes, for example, neutral lipids, they generally lag in their capacity to ionize and analyze larger biomacromolecules, particularly proteins, compared to conventional MALDI.

Chemical aberrations can also stem from factors associated with limitations of the mass analyzer, most importantly, from its mass accuracy and resolution. Lack of sufficient mass accuracy and resolution can result in determining the m/z with some error and the inability to distinguish close to isobaric ions (see Figure 1B). For example, the principles of m/z measurement in an Orbitrap impose fundamental limitations that can compromise its mass resolution and mass accuracy resulting in chemical aberration. Space charge effects in an overfilled Orbitrap can affect the measured frequency of their axial oscillations, thus reducing the mass accuracy and resolution.[65]

2.1.2 | Sample preparation

Even with superior instrumentation, the spatial distribution and chemical information acquired in MSI depend largely on sample collection and preparation prior to imaging. Some of the chemical information can be distorted if proper care is not taken during sample preparation. For example, the turnover rate for important metabolites in metabolically active specimens, such as adenosine triphosphate and glucose 6-phosphate, can be on the order of 1 s.[66] Such chemical aberrations can be typically minimized by following sample preparation steps that are designed to preserve the sample, such as snap freezing in liquid nitrogen, and, less commonly, heat stabilization that slow down and halt endogenous enzymatic breakdown of analytes, respectively.[7]

2.2 | Spatial aberrations

Spatial aberrations are defined as distortions of the true distributions of molecules in the sample described by a coordinate transformation tensor, $\mathbf{T}(\mathbf{x};\boldsymbol{\mu})$, with a parameter vector, $\boldsymbol{\mu}$, due to, for example, stretching or tearing of the tissue section. The transformation tensor connects the undistorted concentration distributions, $c_i(\mathbf{x})$, to the reconstructed ion intensity distributions, $I_i(\mathbf{T}(\mathbf{x};\boldsymbol{\mu}'))$, via $c_i(\mathbf{x}) = F(I_i(\mathbf{T}(\mathbf{x};\boldsymbol{\mu}')), \ldots, I_j(\mathbf{T}(\mathbf{x};\boldsymbol{\mu}')))$, similarly to an image registration process, where optimized parameter values, $\boldsymbol{\mu}'$, are determined by seeking the best match with the undistorted distribution[67]:

$$\boldsymbol{\mu}' = \arg\min_{\boldsymbol{\mu}} C(\boldsymbol{\mu}).$$

Here, $C(\boldsymbol{\mu})$ is the cost function gauging the difference between the undistorted and reconstructed distributions.

Instrumentation, sample preparation, and the sample itself can all contribute to spatial aberrations in MSI. Additionally, some of the factors mentioned below that can lead to spatial aberrations in MSI, for example, sample collection and preparation, also hold true for other molecular imaging modalities, such as fluorescence microscopy and immunostaining.

2.2.1 | Instrumentation

An important instrumental factor that can lead to aberrations is the spatial resolution (lateral and depth) of the imaging technique. Any instrumental limitation that affects the spatial resolution can lead to spatial aberration. Poor spatial resolution in MSI can lead to pixelated

chemical images and to missing the fine details of the molecular distributions throughout the sample.

For LDI-MSI in the scanning microprobe mode, the best attainable lateral spatial resolution is dependent on the focal spot diameter. Thus, for conventional focusing optics, it is diffraction limited. Accordingly, for a laser beam with wavelength of λ, the smallest analysis spot size is defined by the smallest Airy disk diameter, $2R$, that in turn depends on the focal length, f, and the aperture diameter, d, for the focusing lens, $2R = (4\lambda/\pi)(f/d)$. The depth resolution is limited by the depth of focus (DOF) expressed as $\text{DOF} = (8\lambda/\pi)(f/d)^2$ for a Gaussian beam. The diffraction limited focal spot size for an $f = 100$ mm lens with a $d = 10$ mm aperture focusing a Gaussian beam with $\lambda = 337$ nm is $2R = 4.3$ μm and DOF = 85.8 μm. Shorter focal-length and larger numerical aperture lenses can be used for laser ablation in transmission geometry, leading to higher diffraction-limited spatial resolution. The diffraction limit can be sidestepped in near field regime, for example, by delivering the laser light through a sharpened optical fiber.[68] Smaller beam spot size, however, results in less material sampling and, thus, a rapid drop in sensitivity.

Inconsistencies in sampling by the laser beam during LDI-MSI can also lead to spatial aberrations. Examples of instrumental factors that can cause inconsistent sampling include defects in stage movement and nonuniformity of the imaging platform surface.

2.2.2 | Inherent sample properties

The endogenous chemical and physical properties of the sample can influence the ionization and, thus, detection of compounds during imaging. The chemical heterogeneity of the sample, for example, salt concentration gradients across biological tissue sections, can lead to undesired "matrix effects" that affect the ionization efficiency of endogenous compounds (see Figure 1C). For example, higher concentrations of alkali cations in certain regions of the tissue section can enhance adduct formation for certain compounds, giving the false impression that their innate biological levels are relatively higher in these spots (see Figure 1C). Similarly, the extent of competition between endogenous analytes for charges can vary from spot to spot in the sample and affect their detection. These factors present significant limitations especially in quantitative MSI.

Several approaches have been proposed to mitigate complications associated with matrix effects in MSI. To address matrix effects stemming from heterogeneous alkali ion concentrations in biological tissue sections, desalting prior to MSI has been proposed, thus diminishing the abundance variations for these cations throughout the sample.[69] Another strategy used to account for matrix effects in MSI involves normalizing analyte ion intensities to the signals of corresponding internal standards.[70]

Heterogeneity in physical properties of the sample, for example, tensile strength and porosity, can affect the observed spatial distribution of ions. For example, in desorption electrospray ionization MSI, surface conductivity and roughness can both influence ion signal considerably.[71]

2.2.3 | Sample preparation

Sample collection and preparation are critical steps that can significantly influence the observed spatial distribution during imaging. For example, small molecules in a freshly harvested tissue left at near-room temperature can diffuse to significant distances, and their original spatial distributions can be altered. The distance traveled during diffusion can be approximated by the diffusion length, $x = (2Dt)^{1/2}$, where D is the diffusion coefficient and t is the elapsed time. For example, in human tissue that sits for 10 min at 20°C, glucose ($D = 1.6 \times 10^{-6}$ cm^2/s) can diffuse for an approximate distance of $x \approx 440$ μm. To put this number in perspective, if the average mammalian cell size is ~15 μm, glucose can spread over a distance equivalent to ~29 cells under these conditions.

To minimize these artifacts, samples are commonly snap frozen in a cryogen, for example, liquid nitrogen. However, depending on the tissue, this approach can induce fractures that can also distort the native spatial distribution of molecules. One possible way to mitigate this issue is slow freezing of the tissue by placing it on the surface of a prechilled aluminum sheet, followed by loose wrapping and complete immersion in the cryogen.

Factors that can result in spatial aberrations extend beyond sample collection. Even for tissues that are collected under conditions that maximize preservation of morphological features and chemical information, subsequent sample preparation steps can introduce spatial aberrations. In particular, tissue sectioning, handling of the sections, and thaw-mounting them onto the imaging platform can all influence the observed distribution of compounds (see Figure 1D). For example, preparing thin tissue cryosections under suboptimal temperatures or using anti-roll plates with structural defects may introduce folds and tears to the sections (see Figure 1D).

As it is difficult to manipulate the tissue sections to remove these distortions, it might be necessary to use image processing, particularly, image registration,[67] to minimize these spatial aberrations. For example, by taking an optical image of the sample surface prior to sectioning and an image of the distorted tissue section, the former can

be used as a reference to realign the latter using the optimal geometrical transformation, $\mathbf{T}(\mathbf{x};\boldsymbol{\mu}')$ (see Figure 1D). Finding this transformation will depend on the types of spatial distortions (eg, tears, horizontal shear, or translation) that occurred between the two images. The optimal transformation can in turn be used to realign the ion intensity voxels in the image, $I_i(\mathbf{x})$, thus accounting for the spatial aberrations and providing a more accurate representation of the ion spatial distribution, $I_i(\mathbf{T}(\mathbf{x};\boldsymbol{\mu}'))$ (see Figure 1D).

Other important sample preparation steps that can introduce spatial aberrations in MSI include analyte smearing over the tissue surface during sectioning and matrix application in MALDI. The former can be minimized by finding the optimal temperature during sectioning that keeps the tissue frozen without introducing tears. Analyte spreading caused by matrix application is a common problem in sample preparation prior to MALDI imaging, and has been discussed extensively in previous reviews, along with approaches that can minimize it.[7]

3 | INORGANIC AND NANOPHOTONIC PLATFORMS FOR MSI BASED ON LDI

Although a wide variety of inorganic materials have been developed for LDI-MS, only a few of them have been broadly explored in MSI. In this section, these platforms will be categorized based on their chemical composition, mainly, carbon, silicon, metals, metal oxides, and inorganic-organic hybrid substrates/matrices. Additionally, a brief section is assigned to emerging inorganic substrates for LDI-MS that hold potential imaging capabilities, namely, MOFs. Notable applications and main advantages in MSI will be discussed for these techniques. As the ionization processes involved in nanophotonic imaging platforms are fundamentally different, MSI based on these approaches will be discussed separately.

3.1 | MSI by LDI from inorganic substrates and matrices

3.1.1 | Carbon-based platforms

One of the earliest inorganic matrices for LDI-MSI utilized colloidal graphite (graphite-assisted LDI) for molecular imaging of cerebrosides and sulfatides in rat brain tissue sections.[22] The surface of the tissue section was coated with a dilute solution of colloidal graphite using an airbrush, followed by laser irradiation in a raster. The produced chemical images illustrated cerebroside-rich and cerebroside-deficient areas across the surface of the brain tissue section. The study also demonstrated a clear advantage in utilizing colloidal graphite for the detection and spatial mapping of cerebrosides in complex lipid mixtures compared to MALDI with DHB as the matrix.[22] The same technique and sample preparation were also employed in MSI of small metabolites, phenolic compounds, and fatty acids in fruit tissue sections.[72] Additionally, as molecules are desorbed and ionized from the sample surface upon laser irradiation, compounds can be spatially mapped in intact tissues. This was demonstrated in profiling and imaging of plant metabolites by graphite-assisted LDI-MSI from intact leaves and petals.[23] Despite the ionization enhancement for cerebrosides by colloidal graphite, the application of the matrix by spraying the solution onto the sample surface can lead to spreading of analytes soluble in the isopropyl alcohol solvent and, thus, to inaccurate representation of the native molecular spatial distributions. As described later, solvent-free inorganic matrix application under dry conditions can minimize the spatial aberrations associated with spray-based methods.

Other carbon-based materials have been also developed as matrices for LDI-MSI, such as two-dimensional graphene,[73] carbon nanotubes,[74] and carbon dots.[75] In some of these applications, the matrix, for example, nitrogen- and sulfur-doped carbon dots, was sprayed on top of the sample surface that was then interrogated with a laser for the spatial profiling of small metabolites, such as endocrine-disrupting chemicals in animal tissue sections.[75] In a different application, the generation of carbon clusters in negative ion mode LDI-MS was exploited to map the sub-organ spatial distribution of carbon nanomaterials, for example, carbon nanotubes, in animal tissue sections.[74]

Compared to silicon- and metal-based platforms, carbon-based substrates have been less used for imaging applications. One of the main reasons for their limitations is that carbon nanomaterials, for example, carbon nanotubes, can be dislodged from the substrate during desorption, causing contamination of the mass spectrometer and potential instrumental breakdown.[76]

3.1.2 | Silicon nanostructures

Based on the success of NIMS for trace analysis, it was also utilized for molecular imaging. This platform consists of an etched silicon substrate with ~10-nm pores to trap molecules, such as siloxanes, that are called “initiators.” Rapid surface heating from laser irradiation results in initiator vaporization from the clathrates, causing desorption and ionization of adsorbed materials. Because NIMS is a matrix-free platform, spatial aberrations that are commonly encountered in MALDI, such as compromised

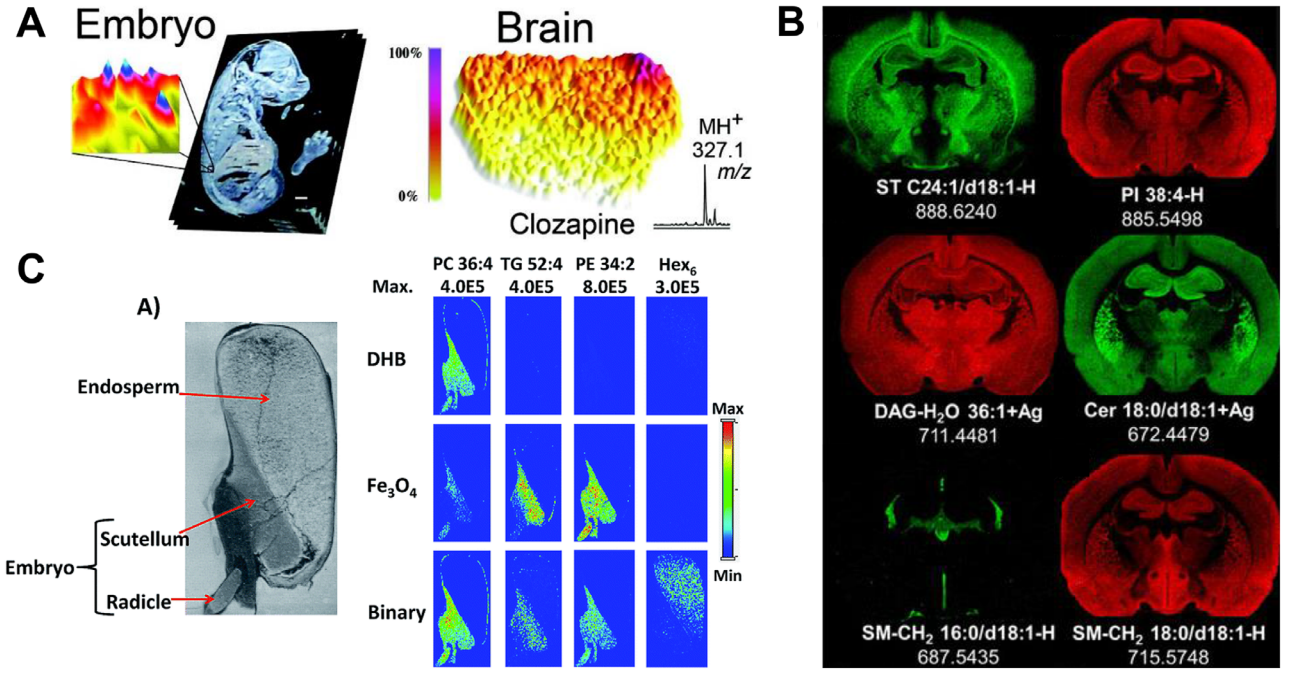

FIGURE 2 **(A)** Ion intensity images obtained by NIMS-LDI-MS for an unspecified compound (left) and clozapine (right) in a mouse embryo and brain tissue sections, respectively. Adapted with permission.[56] Copyright 2011, American Chemical Society. **(B)** Spatial distributions for different lipids acquired by MALDI-MSI using AgNP in rat brain tissue sections. Adapted with permission.[36] Copyright 2017, American Chemical Society. **(C)** Optical image of a maize seed section and ion images for three different lipids (PC, TG, and PE) and an oligosaccharide (Hex_6) obtained by MALDI-MSI using DHB, Fe_3O_4 NP, and a binary matrix consisting of the previous two matrices. Adapted with permission.[87] Copyright 2016, Royal Society of Chemistry

resolution due to analyte diffusion during wet deposition of the matrix and crystal size effects, are not present in NIMS, thus supporting higher lateral resolution with smaller laser beam diameters (15-20 μm).[30,56] This feature confers higher fidelity in the spatial mapping of compounds by providing finer details in the corresponding chemical images. Further reduction in the size of the interrogated region can be achieved in NIMS by using focused ion beams (eg, Au^+, Ga^+, and Bi^+) instead of lasers.[30] Imaging applications for NIMS included detection and spatial mapping of metabolites in tissue sections from mouse embryos (see Figure 2A),[30] normal and cancerous human breast tissue,[56] xenobiotics from mouse brain (see Figure 2A),[58] and biomarkers to aid in distinguishing between different bacterial colonies.[59]

In NIMS, the porous silicon wafer also serves as a substrate for chemical profiling and imaging of the tissue. As many of the analyzed molecules in NIMS reside at the silicon-specimen interface, in cases where it is difficult to obtain sufficiently thin (<10 μm) tissue sections, initially high-fluence (~400 mJ/cm^2) ablation of the sample surface is required in order to remove enough of the sample so the remaining thin section can be interrogated with lower laser fluence (~10 mJ/cm^2).[30]

Generally, for some inorganic substrates and matrices, LDI-MSI requires higher laser fluence (eg, ~50 mJ/cm^2) relative to conventional MALDI (eg, ~20 mJ/cm^2 for α-cyano-4-hydroxycinnamic acid). Under high laser fluence, unknown in-source fragments generated from thermally labile compounds that are prone to fragmentation introduce chemical aberrations by obscuring molecular assignments and the spatial distribution of the parent ions. To address this issue, fluorinated AuNP were introduced in NIMS to attenuate the laser energy, and as reagents for another imaging modality, X-ray computed tomography.[77] This enabled reduced molecular fragmentation, and allowed acquisition of anatomical and chemical information from the same sample via different imaging modalities.

DIOS has also been used for LDI-MSI, albeit for a smaller number of applications. In particular, porous silicon nanostructures functionalized with fluorinated silane groups were used as a substrate for direct LDI-MSI of endogenous, for example, cholesterol, and exogenous, for example, methamphetamine, compounds in fingerprint sweat.[78]

3.1.3 | Metal and metal oxide NP

Metal and metal oxide nanostructures, including NP, can exhibit local enhancement of electromagnetic field

through surface plasmon resonance that can reach orders of magnitude higher field strengths than the incident radiation.[79,80] This phenomenon has given these NP a powerful role as optical antennas in biosensing,[79] spectroscopic (eg, fluorescence) imaging,[81] and laser ablation and ionization,[68] thus paving the way for their applications in LDI-MSI.

Various noble metal NP were developed as substrates and matrices for LDI and used in numerous imaging applications. Both AgNP and AuNP have found novel applications in molecular imaging of certain lipid classes. An advantage of using alkylamine-derivatized AuNP as a matrix in MSI was demonstrated by the enhancement in the detection and localization of glycosphingolipids in mouse brain tissue sections.[54] The derivatized AuNP demonstrated ~20 times higher sensitivity for these compounds compared to MALDI with DHB. Similarly, AgNP implanted into different tissue sections by magnetron sputtering, for example, rat retina, heart, kidney, and brain, were used to profile and image neutral lipids, such as triacylglycerols (TGs), diacylglycerols, and ceramides (see Figure 2B).[33,34,36] This technique provided higher sensitivity for these lipids over MALDI, especially in the presence of phosphatidylcholines (PCs) in the tissue.[33] Implantation of NP in the tissue by magnetron sputtering under dry conditions can avert spatial aberrations associated with other matrix application approaches, such as heterogeneous particle deposition onto the sample surface by spraying NP suspensions.

AuNP have been used as target enhancers for imaging metabolic biomarkers in renal cell carcinoma.[35] Rather than irradiating the tissue directly with a laser beam, materials were transferred from the tissue to the AuNP-based platform through physical contact between the two surfaces. Based on comparisons between chemical images from malignant and healthy samples, some compounds, for example, diacylglyceride and octadecanamide, were selected as potential biomarkers for renal cell carcinoma.[35] In cases where the physical properties of the tissue section vary significantly across the region of interest, the surface-transfer approach may circumvent spatial aberrations that can stem from biased material sampling by the laser. However, as with sample preparation in general, chemical and spatial aberrations, for example, analyte degradation and displacement, may occur during the surface-transfer process.

In addition to biological tissue sections, the versatility of AgNP and AuNP in MSI was demonstrated by the analysis of nonbiological samples and latent fingerprints on different materials (eg, plastic and paper). To minimize analyte diffusion caused by NP deposition and to improve the spatial distribution, a solvent-free approach involving ion sputtering of AuNP onto fingerprints and counterfeits was adopted.[53] Ion intensities for small metabolites and fatty acids were spatially profiled by LDI-MSI in latent fingerprints, whereas minimally destructive and simultaneous imaging of several compounds in counterfeit banknotes revealed the use of different ink dyes.[53]

Large-scale screening of the ionization efficiencies for various small molecules using different NP provided a systematic guide for selecting certain materials for the analysis and imaging of specific compounds.[82] For example, comparative LDI-MSI of plant root cross sections sputter-coated with six types of metal NP demonstrated differential ionization and spatial profiling of metabolites and lipids.[83] Ag, Au, and Pt appeared to be the most effective NP for imaging a broader range of compounds compared to Cu, Ni, and Ti.[83]

Despite notable advantages in using noble metal NP, such as ionization enhancement for small molecules and neutral lipids, the laser ablation/desorption plume generated from these platforms can sometimes contain metal ion clusters (eg, Au_n^+) that may interfere with the ionization and detection of other compounds. In contrast, metal oxides, particularly, TiO_2 NP[84,85] and chemically modified TiO_2 monoliths,[38,40] have been shown to be relatively more stable LDI matrices/substrates. A comparison among AuNP, DHB, and TiO_2 NP as matrices in LDI-MSI of mouse brain tissue sections showed that the latter provided higher signal intensities and improved spatial localization for some low-molecular-weight species, potentially due to ion suppression by DHB and Au_n^+.[84] More recently, sub-micron TiO_2 monoliths modified with dopamine were developed as an imaging platform with enhanced sensitivity for small molecules and Lewis basic lipids from aging mouse brain tissue sections compared to TiO_2 NP,[38] and as a solid phase for analyte imprinting and quantitative imaging.[40] Metal oxide functional NP (fNP) based on hematite and functionalized silicate were used for MSI of lipids and peptides in rat brain tissue sections with high spatial resolution.[55] The small diameter of the fNP (d = 3.7 nm) enabled molecular imaging with improved spatial resolution (~15 μm).

Laser-engineered quasiperiodic AR microstructures composed of semiconductor (silicon), metal (eg, copper), and stainless steel NP have been recently developed as inorganic platforms for LDI-MS, given their high light-to-heat conversion efficiency (97 %) in the UV region.[16,43,44] By coating the latter surfaces with polydopamine, the sensitivity of these platforms can be enhanced owing to the high UV absorption of the coating and the resulting lower heat dissipation in the substrate.[44] Polydopamine-coated AR stainless steel substrates have been used for LDI-MSI of lipids in mouse brain and liver tissue sections, such as TGs, PCs, and phosphatidylethanolamines (PEs).[44]

3.1.4 | Hybrid LDI platforms

The inherent chemical complexity of biological samples, particularly, variations in the competition for charges across a tissue section, can have dramatic effects on the molecular coverage and can lead to spatial aberrations. Organic and inorganic matrices/substrates have been shown to be complementary to each other with regard to preferential ionization and detection of different classes of compounds.[86] For example, although ionization of TGs is significantly suppressed in the presence of PCs using several organic matrices in MALDI, they can be selectively ionized by some inorganic matrices, for example, AgNP and Fe_3O_4 NP.[33,87] Thus, to expand the molecular coverage from complex biological tissue sections and to obtain more accurate spatial distributions for competing analytes, organic-inorganic hybrid matrices have been developed and implemented in MSI.

A binary matrix consisting of DHB and Fe_3O_4 NP has been used to reduce bias toward ionization of certain molecular classes over others, for example, PCs and TGs from maize seed sections, thus providing simultaneous spatial profiling for these lipids (see Figure 2C).[87] It is worth noting that for some compounds, for example, PEs, TGs, and digalactosyldiacylglycerols, the ion intensities observed with the binary matrix were still lower compared to using Fe_3O_4 NP alone (see Figure 2C).[87] In contrast, the binary matrix has been demonstrated to significantly enhance ionization of oligosaccharides compared to using either of the two matrices alone (see Figure 2C).[87]

In a different application, SiO_2 NP were used as 9-aminoacridine carriers to induce controlled release of the organic matrix from the NP upon exposure to ammonia vapors.[88] An advantage of this approach is the reduction in analyte spreading over the sample surface as it can often happen when applying organic matrices for conventional MALDI using spray-based methods. This enabled LDI-MSI with spatial resolution of ~10 μm for single-algal-cell imaging.[88]

3.1.5 | Metal organic frameworks

More recently, MOFs have emerged as an LDI platform with special characteristics, including crystalline structure with highly uniform porosity, flexible geometrical designs, structural rigidity, and large surface area.[89] MOFs promoted excellent ionization in positive and negative ion polarity with clean background.[46] The wide variety of combinations between the metals and ligands in MOFs makes it possible to selectively enhance the ionization for certain compounds. For example, phosphopeptide detection can be enhanced by using zirconium-based MOFs given their high affinity to phosphorus-containing groups.[90]

Although no imaging capabilities have been demonstrated yet for MOFs, some of their special characteristics, particularly, their highly uniform crystalline structures and clean spectral background, confer promising advantages in MSI applications.

3.2 | MSI by LDI from nanophotonic platforms

When the critical dimensions of a nanostructure become commensurate with the wavelength of the laser radiation, their interaction can no longer be described by conventional optics. Instead, these nanophotonic interactions can exhibit new properties, for example, field enhancement in the vicinity of the nanostructure, and the abolition of the diffraction limit. Nanophotonic ionization relies on such structures, for example, laser-induced microcolumn arrays, silicon NAPAs, and elevated bowtie (EBT) arrays, and benefits from these special interactions.[16,17,91] More generally, when the critical dimensions of a nanostructure are shorter than the characteristic lengths for various forms of energy transport, the ensuing energy confinement results in new forms of ion production.[63]

In the case of the most studied nanophotonic ionization platform, NAPA, the periodicity of the nanoposts is commensurate with the wavelength of the UV laser radiation.[17] The strongest evidence for ion production based on nanophotonic interactions in NAPA-LDI comes from the dramatic drop in ion yields to zero as the light polarization angle is changed from p-polarized to s-polarized at a constant fluence (see Figure 3A).[17] Another nanophotonic ionization platform, the EBT array, is derived from NAPA by positioning chromium bowtie antennas on top of silicon nanopost pairs. These structures require lower laser fluence threshold for ionization, and, thus, they can produce higher ion yields compared to NAPA-LDI through enhanced near-field effects at the gaps in the bowties.[91]

In NAPA-LDI-MSI, the biological tissue section is placed on top of the nanoposts and irradiated by UV laser pulses. The radiation penetrates the tissue and interacts with underlying nanoposts, leading to near-field enhancement of the incident laser intensity and heating of the posts, resulting in desorption and ionization of tissue material (see Figure 3B). The absence of matrix deposition during NAPA imaging minimizes the chemical and spatial perturbations in the sample, and the highly uniform array of nanoposts reduces substrate-induced biases, or "hot spots," during sampling that can occur in other nonuniform platforms.

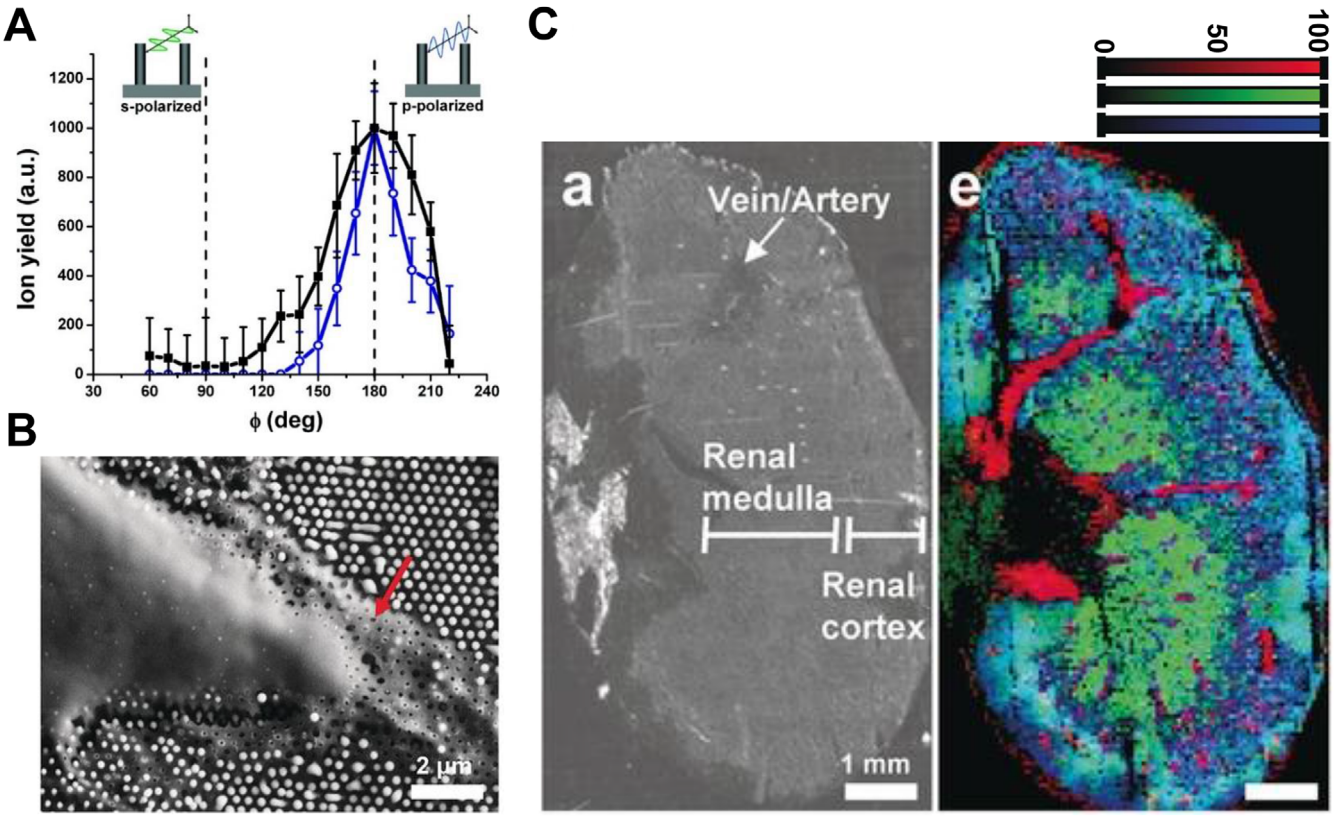

FIGURE 3 **(A)** Dependence of verapamil (■) and bradykinin (○) ion intensities on polarization angle, ϕ, at a constant fluence, in nanophotonic ionization by NAPA. Adapted with permission.[17] Copyright 2010, American Chemical Society. **(B)** Scanning electron microscope (SEM) image of a HepG2/C3A cell on NAPA after laser irradiation, showing pores (see arrow) in the lamellipodia as a result of desorption of cellular material from the nanoposts. Adapted with permission.[60] Copyright 2016, Wiley. **(C)** Combined ion image acquired by NAPA-LDI-MSI for three different chemical species in a mouse kidney tissue section. Adapted with permission.[60] Copyright 2016, Wiley

Molecular imaging capabilities for NAPA were first demonstrated on mouse brain and kidney tissue sections, algal cultures, and lamellipodia of human hepatocarcinoma cells.[60] Glycerophospholipids, sphingolipids, and fatty acids were annotated and spatially profiled throughout the tissue sections (see Figure 3C). More recently, advantages of NAPA in MSI were demonstrated in comparative studies to MALDI imaging of various lipid classes in tissue sections from mouse brain, lung, normal human skin, and hidradenitis suppurativa-affected human skin.[61] Compared to MALDI, NAPA provided significantly enhanced ionization for PEs, phosphatidylethanolamine-plasmalogens, hexosylceramides, and TGs in these complex biological samples.[61]

4 | CONCLUSIONS AND OUTLOOK

Inorganic and nanophotonic structures are emerging LDI platforms for MSI applications. They offer particular advantages for multiplexed imaging, including high sensitivity, wide dynamic range, high molecular coverage for low-mass compounds, no external matrix application, improved spatial resolution, and ionization enhancement for compounds that are typically suppressed in conventional MALDI.

In addition to the chemical and spatial aberrations for MSI discussed above, several challenges remain. Compared to conventional organic MALDI matrices, the synthesis and fabrication of inorganic and nanophotonic platforms is still being developed and is less cost-effective, thus hampering commercialization. These constraints impose limitations on exploring the underlying desorption and ionization mechanisms, and on improving their analytical performance. By exploring the fundamental physical and chemical processes that are involved in these techniques, such as laser-substrate interactions, energy redistribution in the substrate, and desorption and ionization mechanisms, some of the limitations of these platforms may be better understood, and, thus, potential solutions may be devised. These investigations can open opportunities for achieving several desired goals, such as enhanced detection of larger intact biomolecules (eg, proteins), tunable molecular selectivity, improved sensitivity,

reduced chemical and spatial aberrations, and multimodal imaging.

The growing field of single-cell metabolomics, primarily limited by the small sample volume, can benefit from the ultrahigh sensitivity for some of the inorganic and nanophotonic LDI platforms, for example, 800 ymol for silylated porous Si and 800 zmol for NAPA-LDI.[27,92] Phenotypic profiling of single cells through metabolomics, combined with single-cell proteomics and single-cell transcriptomics, raises the prospect of developing single-cell systems biology. Additionally, as with quantitative MSI, the extent of ion signal variation stemming from the analytical technique is a crucial part in single-cell analysis. Cellular heterogeneity, an inherent biological phenomenon, can be explored when the ion signal variations associated with the technique are negligible compared to those stemming from biological fluctuations. Thus, as some technical factors that can amplify the signal variations, such as inhomogeneous matrix-analyte cocrystallization in MALDI, are absent in some of these inorganic platforms (eg, NAPA), cellular heterogeneity can be explored with higher fidelity.

Quantitative MSI, a highly desired goal, can be further improved by developing methods that address key limitations, for example, ion signal dependence on chemical and morphological sample properties. Combining these aspired breakthroughs with the high sensitivity, wide dynamic range, and high surface uniformity for some of these inorganic platforms offers reproducible sampling with a high fidelity for quantitation.

CONFLICT OF INTEREST

The authors declare no conflict of interest.

ACKNOWLEDGMENT

This work is supported by the U.S. National Science Foundation, Plant Genome Program under grant no. IoS-1734145.

ORCID

Laith Z. Samarah https://orcid.org/0000-0003-1358-2727

Akos Vertes https://orcid.org/0000-0001-5186-5352

REFERENCES

1. A. R. Kherlopian, T. Song, Q. Duan, M. A. Neimark, M. J. Po, J. K. Gohagan, A. F. Laine, *BMC Syst. Biol.* **2008**, *2*, 74.
2. J. M. Chabala, K. K. Soni, J. Li, K. L. Gavrilov, R. Levisetti, *Int. J. Mass Spectrom. Ion Process.* **1995**, *143*, 191.
3. L. A. McDonnell, R. M. A. Heeren, *Mass Spectrom. Rev.* **2007**, *26*, 606.
4. N. Winograd, *Anal. Chem.* **2005**, *77*, 142A.
5. K. Tanaka, H. Waki, Y. Ido, S. Akita, Y. Yoshida, T. Yoshida, *Rapid Commun. Mass Spectrom.* **1988**, *2*, 151
6. a) R. M. Caprioli, T. B. Farmer, J. Gile, *Anal. Chem.* **1997**, *69*, 4751; b) M. Stoeckli, P. Chaurand, D. E. Hallahan, R. M. Caprioli, *Nat. Med.* **2001**, *7*, 493.
7. J. L. Norris, R. M. Caprioli, *Chem. Rev.* **2013**, *113*, 2309.
8. Y. C. Ho, M. C. Tseng, Y. W. Lu, C. C. Lin, Y. J. Chen, M. R. Fuh, *Anal. Chim. Acta* **2011**, *697*, 1.
9. A. R. Buchberger, K. DeLaney, J. Johnson, L. J. Li, *Anal. Chem.* **2018**, *90*, 240.
10. R. J. A. Goodwin, *J. Proteom.* **2012**, *75*, 4893.
11. a) F. G. Hopwood, L. Michalak, D. S. Alderdice, K. J. Fisher, G. D. Willett, *Rapid Commun. Mass Spectrom.* **1994**, *8*, 881; b) Y. C. Chen, J. Y. Wu, *Rapid Commun. Mass Spectrom.* **2001**, *15*, 1899; c) Z. X. Shen, J. J. Thomas, C. Averbuj, K. M. Broo, M. Engelhard, J. E. Crowell, M. G. Finn, G. Siuzdak, *Anal. Chem.* **2001**, *73*, 612; d) C. C. Pei, C. Liu, Y. Wang, D. Cheng, R. X. Li, W. K. Shu, C. Q. Zhang, W. L. Hu, A. H. Jin, Y. N. Yang, J. J. Wan, *Angew. Chem. Int. Ed.* **2020**, *59*, 10831.
12. J. Sunner, E. Dratz, Y. C. Chen, *Anal. Chem.* **1995**, *67*, 4335.
13. J. Wei, J. M. Buriak, G. Siuzdak, *Nature* **1999**, *399*, 243.
14. T. Kinumi, T. Saisu, M. Takayama, H. Niwa, *J. Mass Spectrom.* **2000**, *35*, 417.
15. S. Y. Xu, Y. F. Li, H. F. Zou, J. S. Qiu, Z. Guo, B. C. Guo, *Anal. Chem.* **2003**, *75*, 6191.
16. B. N. Walker, T. Razunguzwa, M. Powell, R. Knochenmuss, A. Vertes, *Angew. Chem. Int. Ed*. **2009**, *48*, 1669.
17. B. N. Walker, J. A. Stolee, D. L. Pickel, S. T. Retterer, A. Vertes, *J. Phys. Chem. C* **2010**, *114*, 4835.
18. J. A. Stolee, Y. Chen, A. Vertes, *J. Phys. Chem. C* **2010**, *114*, 5574.
19. a) L. Huang, J. J. Wan, X. Wei, Y. Liu, J. Y. Huang, X. M. Sun, R. Zhang, D. D. Gurav, V. Vedarethinam, Y. Li, R. P. Chen, K. Qian, *Nat. Commun.* **2017**, *8*, 220; b) X. M. Sun, L. Huang, R. Zhang, W. Xu, J. Y. Huang, D. D. Gurav, V. Vedarethinam, R. P. Chen, J. T. Lou, Q. Wang, J. J. Wan, K. Qian, *ACS Cent. Sci.* **2018**, *4*, 223; c) W. K. Shu, Y. Wang, C. Liu, R. X. Li, C. C. Pei, W. H. Lou, S. H. Lin, W. Di, J. J. Wan, *Small Methods* **2020**, *4*, 1900469.
20. a) Z. Takats, J. M. Wiseman, B. Gologan, R. G. Cooks, *Science* **2004**, *306*, 471; b) M. Haapala, J. Pol, V. Saarela, V. Arvola, T. Kotiaho, R. A. Ketola, S. Franssila, T. J. Kauppila, R. Kostiainen, *Anal. Chem.* **2007**, *79*, 7867; c) P. Nemes, A. Vertes, *Anal. Chem.* **2007**, *79*, 8098; d) L. C. Chen, K. Yoshimura, Z. Yu, R. Iwata, H. Ito, H. Suzuki, K. Mori, O. Ariyada, S. Takeda, T. Kubota, K. Hiraoka, *J. Mass Spectrom.* **2009**, *44*, 1469; e) Y. Coello, A. D. Jones, T. C. Gunaratne, M. Dantus, *Anal. Chem.* **2010**, *82*, 2753.
21. a) S. Alimpiev, S. Nikiforov, V. Karavanskii, T. Minton, *J. Sunner, J. Chem. Phys.* **2001**, *115*, 1891; b) S. L. Walton, D. J. Mitchell, *J. Radioanal. Nucl. Chem.* **2013**, *296*, 1113.
22. S. W. Cha, E. S. Yeung, *Anal. Chem.* **2007**, *79*, 2373.
23. S. W. Cha, H. Zhang, H. I. Ilarslan, E. S. Wurtele, L. Brachova, B. J. Nikolau, E. S. Yeung, *Plant J.* **2008**, *55*, 348.
24. a) C. S. Pan, S. Y. Xu, L. G. Hu, X. Y. Su, J. J. Ou, H. F. Zou, Z. Guo, Y. Zhang, B. C. Guo, *J. Am. Soc. Mass Spectrom.* **2005**, *16*, 883; b) D. Nanjo, K. Shibamoto, T. Korenaga, *Chem. Lett.* **2009**, *38*, 142; c) C. Y. Shi, C. H. Deng, X. M. Zhang, P. Y. Yang, *ACS Appl. Mater. Interfaces* **2013**, *5*, 7770.
25. a) X. L. Dong, J. S. Cheng, J. H. Li, Y. S. Wang, *Anal. Chem.* **2010**, *82*, 6208; b) C. Y. Shi, J. R. Meng, C. H. Deng, *J. Mater. Chem.* **2012**, *22*, 20778; c) C. Y. Shi, J. R. Meng, C. H. Deng, *Chem. Commun.* **2012**, *48*, 2418; d) Q. H. Min, X. X. Zhang, X. Q. Chen, S. Y. Li, J. J. Zhu, *Anal. Chem.* **2014**, *86*, 9122; e) X. Huang, Q. Liu,

X. Y. Huang, Z. Nie, T. Ruan, Y. G. Du, G. B. Jiang, *Anal. Chem.* **2017**, *89*, 1307; f) Z. Y. Rao, F. L. Geng, Y. Q. Zhou, D. Cao, Y. H. Kang, *Anal. Methods* **2017**, *9*, 2014; g) D. Y. Wang, X. Huang, J. Li, B. He, Q. Liu, L. G. Hu, G. B. Jiang, *Chem. Commun.* **2018**, *54*, 2723.

26. a) D. Hussain, M. Najam-ul-Haq, F. Jabeen, M. N. Ashiq, M. Athar, M. Rainer, C. W. Huck, G. K. Bonn, *Anal. Chim. Acta* **2013**, *775*, 75; b) C. L. Wu, C. C. Wang, Y. H. Lai, H. Lee, J. D. Lin, Y. T. Lee, Y. S. Wang, *Anal. Chem.* **2013**, *85*, 3836; c) J. M. Chitanda, H. X. Zhang, E. Pahl, R. W. Purves, A. El-Aneed, *J. Am. Soc. Mass Spectrom.* **2016**, *27*, 1686; d) L. Zhu, L. H. Yin, J. J. Xue, Z. H. Wang, Z. X. Nie, *ACS Appl. Mater. Interfaces* **2018**, *10*, 41178.
27. S. A. Trauger, E. P. Go, Z. X. Shen, J. V. Apon, B. J. Compton, E. S. P. Bouvier, M. G. Finn, G. Siuzdak, *Anal. Chem.* **2004**, *76*, 4484.
28. a) E. P. Go, J. V. Apon, G. H. Luo, A. Saghatelian, R. H. Daniels, V. Sahi, R. Dubrow, B. F. Cravatt, A. Vertes, G. Siuzdak, *Anal. Chem.* **2005**, *77*, 1641; b) C. W. Tsao, P. Kumar, J. K. Liu, L. Devoe, *Anal. Chem.* **2008**, *80*, 2973; c) C. M. Wang, J. M. Reed, L. Y. Ma, Y. Qiao, Y. Luo, S. L. Zou, J. J. Hickman, M. Su, *J. Phys. Chem. C* **2012**, *116*, 15415.
29. K. P. Law, *Int. J. Mass Spectrom.* **2010**, *290*, 72.
30. T. R. Northen, O. Yanes, M. T. Northen, D. Marrinucci, W. Uritboonthai, J. Apon, S. L. Golledge, A. Nordstrom, G. Siuzdak, *Nature* **2007**, *449*, 1033.
31. a) T. Seino, H. Sato, A. Yamamoto, A. Nemoto, M. Torimura, H. Tao, *Anal. Chem.* **2007**, *79*, 4827; b) H. H. Abdelmaksoud, T. M. Guinan, N. H. Voelcker, *ACS Appl. Mater. Interfaces* **2017**, *9*, 5092.
32. a) S. W. Cha, Z. H. Song, B. J. Nikolau, E. S. Yeung, *Anal. Chem.* **2009**, *81*, 2991; b) J. H. Jun, Z. H. Song, Z. J. Liu, B. J. Nikolau, E. S. Yeung, Y. J. Lee, *Anal. Chem.* **2010**, *82*, 3255; c) J. Niziol, W. Rode, Z. Zielinski, T. Ruman, *Int. J. Mass Spectrom.* **2013**, *335*, 22; d) J. Niziol, T. Ruman, *Anal. Chem.* **2013**, *85*, 12070; e) T. R. Kuo, D. Y. Wang, Y. C. Chiu, Y. C. Yeh, W. T. Chen, C. H. Chen, C. W. Chen, H. C. Chang, C. C. Hu, C. C. Chen, *Anal. Chim. Acta* **2014**, *809*, 97; f) M. R. Yang, T. Fujino, *Chem. Phys. Lett.* **2014**, *592*, 160; g) H. Z. Lai, S. G. Wang, C. Y. Wu, Y. C. Chen, *Anal. Chem.* **2015**, *87*, 2114; h) S. L. Chau, H. W. Tang, K. M. Ng, *Anal. Chim. Acta* **2016**, *919*, 62; i) S. S. Hinman, C. Y. Chen, J. C. Duan, Q. Cheng, *Nanoscale* **2016**, *8*, 1665; j) X. C. Lin, X. N. Wang, L. Liu, Q. Wen, R. Q. Yu, J. H. Jiang, *Anal. Chem.* **2016**, *88*, 9881; k) H. He, Y. R. Wen, Z. C. Guo, P. F. Li, Z. Liu, *Anal. Chem.* **2019**, *91*, 8390.
33. a) S. N. Jackson, K. Baldwin, L. Muller, V. M. Womack, J. A. Schultz, C. Balaban, A. S. Woods, *Anal. Bioanal. Chem.* **2014**, *406*, 1377; b) L. Muller, A. Kailas, S. N. Jackson, A. Roux, D. C. Barbacci, J. A. Schultz, C. D. Balaban, A. S. Woods, *Kidney Int.* **2015**, *88*, 186.
34. A. Roux, L. Muller, S. N. Jackson, J. Post, K. Baldwin, B. Hoffer, C. D. Balaban, D. Barbacci, A. Schultz, S. Gouty, B. M. Cox, A. S. Woods, *J. Neurosci. Methods* **2016**, *272*, 19.
35. J. Niziol, K. Ossolinski, T. Ossolinski, A. Ossolinska, V. Bonifay, J. Sekula, Z. Dobrowolski, J. Sunner, I. Beech, T. Ruman, *Anal. Chem.* **2016**, *88*, 7365.
36. L. Muller, K. Baldwin, D. C. Barbacci, S. N. Jackson, A. Roux, C. D. Balaban, B. E. Brinson, M. I. McCully, E. K. Lewis, J. A. Schultz, A. S. Woods, *J. Am. Soc. Mass Spectrom.* **2017**, *28*, 1716.
37. a) C. Rejeeth, X. C. Pang, R. Zhang, W. Xu, X. M. Sun, B. Liu, J. T. Lou, J. J. Wan, H. C. Gu, W. Yan, K. Qian, *Nano Res.* **2018**, *11*, 68; b) D. D. Gurav, Y. Jia, J. Ye, K. Qian, *Nanoscale Adv.* **2019**, *1*, 459; c) V. Vedarethinam, L. Huang, W. Xu, R. Zhang, D. D. Gurav, X. M. Sun, J. Yang, R. P. Chen, K. Qian, *Small* **2019**, *15*, 1803051; d) H. Y. Su, T. T. Liu, L. Huang, J. Y. Huang, J. Cao, H. Q. Yang, J. Ye, J. Liu, K. Qian, *J. Mater. Chem. B* **2018**, *6*, 7280; e) S. Wu, L. X. Qian, L. Huang, X. M. Sun, H. Y. Su, D. D. Gurav, M. W. Jiang, W. Cai, K. Qian, *Nano-Micro Lett.* **2018**, *10*, 52.
38. Q. Wu, J. L. Chu, S. S. Rubakhin, M. U. Gillette, J. V. Sweedler, *Chem. Sci.* **2017**, *8*, 3926.
39. a) M. Kim, J. M. Park, T. G. Yun, J. Y. Noh, M. J. Kang, J. C. Pyun, *ACS Appl. Mater. Interfaces* **2018**, *10*, 33790; b) R. T. Zhang, Q. Qin, B. H. Liu, L. Qiao, *Anal. Chem.* **2018**, *90*, 3863; c) M. J. Kim, T. G. Yun, J. Jung, J. M. Park, J. Y. Noh, J. Song, M. J. Kang, J. C. Pyun, *Anal. Chem.* **2019**, *91*, 11283; d) Y. D. Zhu, N. Gasilova, M. Jovic, L. Qiao, B. H. Liu, L. T. Lovey, H. Pick, H. H. Girault, *Chem. Sci.* **2018**, *9*, 2212.
40. Q. Wu, S. S. Rubakhin, J. V. Sweedler, *Anal. Chem.* **2020**, *92*, 6613.
41. a) T. Watanabe, H. Kawasaki, T. Yonezawa, R. Arakawa, *J. Mass Spectrom.* **2008**, *43*, 1063; b) G. Gedda, H. F. Wu, *Sens. Actuators B Chem.* **2019**, *288*, 667.
42. a) Q. L. Liang, T. Macher, Y. L. Xu, Y. P. Bao, C. J. Cassady, *Anal. Chem.* **2014**, *86*, 8496; b) Q. L. Liang, J. Sherwood, T. Macher, J. M. Wilson, Y. P. Bao, C. J. Cassady, *J. Am. Soc. Mass Spectrom.* **2017**, *28*, 409.
43. J. Yang, H. J. Zhang, J. Jia , X. R. Zhang, X. X. Ma, M. L. Zhong, Z. Ouyang, *Research* **2018**, *2018*, 5439729.
44. J. Yang, W. P. Zhang, H. J. Zhang, M. L. Zhong, W. B. Cao, Z. S. Li, X. Huang, Z. X. Nie, J. M. Liu, P. Li, X. X. Ma, Z. Ouyang, *ACS Appl. Mater. Interfaces* **2019**, *11*, 46140.
45. a) C. P. Fu, S. Lirio, W. L. Liu, C. H. Lin, H. Y. Huang, *Anal. Chim. Acta* **2015**, *888*, 103; b) Z. Lin, W. Bian, J. N. Zheng, Z. W. Cai, *Chem. Commun.* **2015**, *51*, 8785; c) X. Q. Yang, Z. A. Lin, X. P. Yan, Z. W. Cai, *RSC Adv.* **2016**, *6*, 23790; d) Y. J. Chang, S. S. Yang, X. Z. Yu, H. Zhang, W. B. Shang, Z. Y. Gu, *Anal. Chim. Acta* **2018**, *1032*, 91; e) C. W. Fu, S. Lirio, Y. H. Shih, W. L. Liu, C. H. Lin, H. Y. Huang, *Chem. Eur. J.* **2018**, *24*, 9598.
46. H. L. Liu, Y. J. Chang, T. Fan, Z. Y. Gu, *Chem. Commun.* **2016**, *52*, 12984.
47. Q. Liu, Z. Guo, L. He, *Anal. Chem.* **2007**, *79*, 3535.
48. C. L. de Laorden, A. Beloqui, L. Yate, J. Calvo, M. Puigivila, J. Llop, N. C. Reichardt, *Anal. Chem.* **2015**, *87*, 431.
49. A. Tata, C. Montemurro, A. M. Porcari, K. C. Silva, J. B. L. de Faria, M. N. Eberlin, *Drug Test. Anal.* **2014**, *6*, 949.
50. D. N. de Oliveira, M. S. Ferreira, R. R. Catharino, *PLoS One* **2014**, *9*, e90901.
51. K. Qian, L. Zhou, J. Liu, J. Yang, H. Y. Xu, M. H. Yu, A. Nouwens, J. Zou, M. J. Monteiro, C. Z. Yu, *Sci. Rep.* **2013**, *3*, 1415.
52. a) A. Palermo, E. M. Forsberg, B. Warth, A. E. Aisporna, E. Billings, E. Kuang, H. P. Benton, D. Berry, G. Siuzdak, *ACS Nano* **2018**, *12*, 6938; b) S. H. Yang, L. P. Zhan, C. Z. Liu, L. Fu, R. Chen, Z. X. Nie, *Microchem. J.* **2019**, *150*, 104190; c) H. Ageta, S. Asai, Y. Sugiura, N. Goto-Inoue, N. Zaima, M. Setou, *Med. Mol. Morphol.* **2009**, *42*, 16; d) T. Hayasaka, N. Goto-Inoue, N. Zaima, K. Shrivas, Y. Kashiwagi, M. Yamamoto, M. Nakamoto, M. Setou, *J. Am. Soc. Mass Spectrom.* **2010**, *21*, 1446; e) H. W. Tang, M. Y. M. Wong, W. Lam, Y. C. Cheng, C. M. Che, K. M. Ng, *Rapid Commun. Mass Spectrom.* **2011**, *25*, 3690.

53. a) H. W. Tang, W. Lu, C. M. Che, K. M. Ng, *Anal. Chem.* **2010**, *82*, 1589; b) H. W. Tang, M. Y. M. Wong, S. L. F. Chan, C. M. Che, K. M. Ng, *Anal. Chem.* **2011**, *83*, 453.
54. N. Goto-Inoue, T. Hayasaka, N. Zaima, Y. Kashiwagi, M. Yamamoto, M. Nakamoto, M. Setou, *J. Am. Soc. Mass Spectrom.* **2010**, *21*, 1940.
55. S. Taira, Y. Sugiura, S. Moritake, S. Shimma, Y. Ichiyanagi, M. Setou, *Anal. Chem.* **2008**, *80*, 4761.
56. M. P. Greving, G. J. Patti, G. Siuzdak, *Anal. Chem.* **2011**, *83*, 2.
57. K. B. Louie, B. P. Bowen, X. L. Cheng, J. E. Berleman, R. Chakraborty, A. Deutschbauer, A. Arkin, T. R. Northen, *Anal. Chem.* **2013**, *85*, 10856.
58. O. Yanes, H. K. Woo, T. R. Northen, S. R. Oppenheimer, L. Shriver, J. Apon, M. N. Estrada, M. J. Potchoiba, R. Steenwyk, M. Manchester, G. Siuzdak, *Anal. Chem.* **2009**, *81*, 2969.
59. T. N. Moening, V. L. Brown, L. He, *Anal. Methods* **2016**, *8*, 8234.
60. S. A. Stopka, C. Rong, A. R. Korte, S. Yadavilli, J. Nazarian, T. T. Razunguzwa, N. J. Morris, A. Vertes, *Angew. Chem. Int. Ed.* **2016**, *55*, 4482.
61. a) J. A. Fincher, J. E. Dyer, A. R. Korte, S. Yadavilli, N. J. Morris, A. Vertes, *J. Comp. Neurol.* **2019**, *527*, 2101; b) J. A. Fincher, D. R. Jones, A. R. Korte, J. E. Dyer, P. Parlanti, A. Popratiloff, C. A. Brantner, N. J. Morris, R. K. Pirlo, V. K. Shanmugam, A. Vertes, *Sci. Rep.* **2019**, *9*,17508; c) J. A. Fincher, A. R. Korte, J. E. Dyer, S. Yadavilli, N. J. Morris, D. R. Jones, V. K. Shanmugam, R. K. Pirlo, A. Vertes, *J. Mass Spectrom.* **2019**, *55*, e4443.
62. a) C. K. Chiang, W. T. Chen, H. T. Chang, *Chem. Soc. Rev.* **2011**, *40*, 1269; b) C. Y. Shi, C. H. Deng, *Analyst* **2016**, *141*, 2816; c) H. He, Z. C. Guo, Y. R. Wen, S. X. Xu, Z. Liu, *Anal. Chim. Acta* **2019**, *1090*, 1.
63. J. A. Stolee, B. N. Walker, V. Zorba, R. E. Russo, A. Vertes, *PCCP* **2012**, *14*, 8453.
64. J. O. Park, S. A. Rubin, Y. F. Xu, D. Amador-Noguez, J. Fan, T. Shlomi, J. D. Rabinowitz, *Nat. Chem. Biol.* **2016**, *12*, 482.
65. R. H. Perry, R. G. Cooks, R. J. Noll, *Mass Spectrom. Rev.* **2008**, *27*, 661.
66. W. Y. Lu, X. Y. Su, M. S. Klein, I. A. Lewis, O. Fiehn, J. D. Rabinowitz, *Annu. Rev. Biochem.* **2017**, *86*, 277.
67. S. Klein, M. Staring, P. Andersson, J. P. W. Pluim, in *Medical Image Computing and Computer-Assisted Intervention* (Eds: G. Fichtinger, A. Martel, T. Peters), Vol. *6892*, Springer. (549–556). Berlin **2011**.
68. R. Stockle, P. Setz, V. Deckert, T. Lippert, A. Wokaun, R. Zenobi, *Anal. Chem.* **2001**, *73*, 1399.
69. H. Y. J. Wang, H. W. Wu, P. J. Tsai, C. B. Liu, *Anal. Bioanal. Chem.* **2012**, *404*, 113.
70. I. Lanekoff, S. L. Stevens, M. P. Stenzel-Poore, J. Laskin, *Analyst* **2014**, *139*, 3528.
71. Z. Takats, J. M. Wiseman, R. G. Cooks, *J. Mass Spectrom.* **2005**, *40*, 1261.
72. H. Zhang, S. W. Cha, E. S. Yeung, *Anal. Chem.* **2007**, *79*, 6575.
73. W. L. Friesen, B. J. Schultz, J. F. Destino, T. E. G. Alivio, J. R. Steet, S. Banerjee, T. D. Wood, *J. Am. Soc. Mass Spectrom.* **2015**, *26*, 1963.
74. S. M. Chen, C. Q. Xiong, H. H. Liu, Q. Q. Wan, J. Hou, Q. He, A. Badu-Tawiah, Z. X. Nie, *Nat. Nanotechnol.* **2015**, *10*, 176.
75. Z. Lin, J. Wu, Y. Q. Dong, P. S. Xie, Y. Zhang, Z. W. Cai, *Anal. Chem.* **2018**, *90*, 10872.
76. S. F. Ren, L. Zhang, Z. H. Cheng, Y. L. Guo, *J. Am. Soc. Mass Spectrom.* **2005**, *16*, 333.
77. M. E. Kurczy, Z. J. Zhu, J. Ivanisevic, A. M. Schuyler, K. Lalwani, A. F. Santidrian, J. M. David, A. Giddabasappa, A. J. Roberts, H. J. Olivos, P. J. O'Brien, L. Franco, M. W. Fields, L. P. Paris, M. Friedlander, C. H. Johnson, A. A. Epstein, H. E. Gendelman, M. R. Wood, B. H. Felding, G. J. Patti, M. E. Spilker, G. Siuzdak, *Nat. Commun.* **2015**, *6*, 5998.
78. T. Guinan, C. Della Vedova, H. Kobus, N. H. Voelcker, *Chem. Commun.* **2015**, *51*, 6088.
79. P. Muhlschlegel, H. J. Eisler, O. J. F. Martin, B. Hecht, D. W. Pohl, *Science* **2005**, *308*, 1607.
80. A. Agrawal, R. W. Johns, D. J. Milliron, *Ann. Rev. Mater. Res.*, **2017**, *1*, 1.
81. P. Anger, P. Bharadwaj, L. Novotny, *Phys. Rev. Lett.* **2006**, *96*, 113002.
82. G. B. Yagnik, R. L. Hansen, A. R. Korte, M. D. Reichert, J. Vela, Y. J. Lee, *Anal. Chem.* **2016**, *88*, 8926.
83. R. L. Hansen, M. E. Duenas, Y. J. Lee, *J. Am. Soc. Mass Spectrom.* **2019**, *30*, 299.
84. K. Shrivas, T. Hayasaka, Y. Sugiura, M. Setou, *Anal. Chem.* **2011**, *83*, 7283.
85. L. Morosi, P. Spinelli, M. Zucchetti, F. Pretto, A. Carra, M. D'Incalci, R. Giavazzi, E. Davoli, *PLoS One* **2013**, *8*, e72532.
86. K. Nozaki, Y. Nakabayashi, T. Murakami, A. Miyazato, I. Osaka, *J. Mass Spectrom.* **2019**, *54*, 612.
87. A. D. Feenstra, K. C. O'Neill, G. B. Yagnik, Y. J. Lee, *RSC Adv.* **2016**, *6*, 99260.
88. P. H. Li, S. Y. Huang, Y. C. Chen, P. L. Urban, *RSC Adv.* **2013**, *3*, 6865.
89. Y. H. Shih, C. H. Chien, B. Singco, C. L. Hsu, C. H. Lin, H. Y. Huang, *Chem. Commun.* **2013**, *49*, 4929.
90. L. F. Chen, J. J. Ou, H. W. Wang, Z. S. Liu, M. L. Ye, H. F. Zou, *ACS Appl. Mater. Interfaces* **2016**, *8*, 20292.
91. S. A. Stopka, X. A. Holmes, A. R. Korte, L. R. Compton, S. T. Retterer, A. Vertes, *Adv. Funct. Mater.* **2018**, *28*, 1801730.
92. B. N. Walker, J. A. Stolee, A. Vertes, *Anal. Chem.* **2012**, *84*, 7756.

AUTHOR BIOGRAPHIES

Laith Z. Samarah received his BS degree in biology from the American University of Beirut, Beirut, Lebanon, in 2011. He is currently a PhD candidate under the supervision of Professor Akos Vertes at the Department of Chemistry of the George Washington University in Washington, DC, USA. His research interests include the development and implementation of mass-spectrometry-based techniques for single-cell analysis, and matrix-free platforms for laser desorption ionization and chemical imaging of biological tissues.

Akos Vertes is a Professor of Chemistry and a Professor of Biochemistry and Molecular Biology at the George Washington University in Washington, DC, USA. His research interests encompass the development of new analytical techniques applicable in diverse fields of chemistry, biology, and medicine. His research has been presented in over 180 peer-reviewed publications ($h = 46$), and in two books. He is a co-inventor on 19 issued patents. He was elected Fellow of the National Academy of Inventors, and received the Distinguished Researcher Award at GWU, the 2012 Hillebrand Prize, and the Oscar and Shoshana Trachtenberg Prize for Scholarship. He is a Doctor of the Hungarian Academy of Sciences. He served as Visiting Faculty at the Lawrence Berkeley National Laboratory, an MTA Distinguished Guest Scientist at the Hungarian Academy of Sciences in Hungary, and twice as a Visiting Professor at the Swiss Federal Institute of Technology Zurich (ETH Zurich) in Switzerland. He is a Visiting Professor at the Shanghai Jiao Tong University in China.

How to cite this article: Samarah LZ, Vertes A. Mass spectrometry imaging based on laser desorption ionization from inorganic and nanophotonic platforms. *VIEW*. 2020;20200063. https://doi.org/10.1002/VIW.20200063